Mountain waves produced by a stratified shear flow with a boundary layer. Part III: Trapped lee waves and horizontal momentum transport

Clément Soufflet, Francois Lott, Bruno Deremble

This work has been submitted to J. Atmos. Sciences for publication.

Mountain waves produced by a stratified shear flow with a boundary layer. Part III: Trapped lee waves and horizontal momentum transport.

Clément Soufflet, François Lott and Bruno Deremble
Submitted October 4, 2021

Laboratoire de Météorologie Dynamique, PSL Research Institute, Ecole Normale Supérieure, 24 rue Lhomond, 75231 Paris France

ABSTRACT: The boundary layer theory for non-hydrostatic mountain waves presented in Part II is extended to include upward propagating gravity waves and trapped lee waves. To do so, the background wind with constant shear used in Part II is smoothly curved and become constant above a "boundary-layer" height D which is much larger than the inner layer scale δ. As in Part II, the pressure drag stays well predicted by a gravity wave drag when the surface Richardson number $J > 1$ and by a form drag when $J < 1$. As in Part II also, the sign of the Reynolds stress is predominantly positive in the near neutral case ($J < 1$) and negative in the stable case ($J > 1$) but situations characterized by positive and negative Reynolds stress now combine when $J \sim 1$. In the latter case, and even when dissipation produces positive stress in the lower part of the inner layer, a property we associated with form drag in Part II, negative stresses are quite systematically found aloft. These negative stresses are due to upward propagating waves and trapped lee waves, the first being associated with negative vertical flux of pseudo-momentum aloft the inner layer, the second to negative horizontal flux of pseudo-momentum downstream the obstacle. These results suggest that the significance of mountain waves for the large scale flow is more substantial than expected and when compared to the enhancement of the boundary layer form drag by the mountain.

Introduction

Low-level orographic drag which results from the interaction between mountain waves and the atmospheric boundary layer has a significant impact on the general circulation of the atmosphere (Pithan et al. (2016), Elvidge et al. (2019)). However, this interaction is still not well understood and thus not well represented in climate models (see (Lott et al. 2020a,b); Part I and II henceforth). In fact, the impact of mountains on the boundary layer and the mountain gravity waves dynamics are actually handled by two distinct parameterizations: one for neutral flows (or small mountains), and one for stably stratified flow (or big mountains) (Beljaars et al. 2004; Lott and Miller 1997, Part I and II). In this three part study, we are trying to unify the theory of flow-topography interaction in the different regimes. Parts I and II focused on the case where the background wind vanishes at the surface, and where the background wind shear u_{0_z} and stratification N^2 are constant. In this context, dissipation controls the dynamics over an inner layer which thickness is about 5 times the "inner" layer scale

$$\delta = \left(\frac{\nu L}{u_{0_z}}\right)^{\frac{1}{3}}, \tag{1}$$

with L the characteristic length of the obstacle, and ν the constant viscosity coefficient. We recall that we develop our framework with constant viscosity. This hypothesis probably overstates dissipation but permits a comprehensive description of the interaction.

Corresponding author: François Lott,flott@lmd.ens.fr

In Part I, we analyzed the wave-boundary layer interaction in the hydrostatic case and showed that for small mountains the wave stress is extracted from the inner layer instead of the ground surface as in the inviscid case: the large-scale flow is accelerated near the surface within the inner layer to balance the gravity wave drag. We also showed that the surface pressure drag and the Reynolds stress amplitude are well predicted using linear inviscid gravity wave theory as long as we take for the incident wind its value around the inner layer scale.

In Part II we examined the non-hydrostatic case, in order to study the transition from stratified conditions to neutral conditions (small Richardson number). In the neutral case, we found that surface drag is well predicted by a form drag and that the Reynolds stress profile is maximum near the top of the inner layer indicating that the mean flow is decelerated in the lower part of the inner layer and accelerated in the upper part. For more stable flows (larger Richardson number), we recover the results from part I for which internal waves control the dynamics: the surface pressure drag is well predicted by a wave drag, and the Reynolds stress accelerates the large-scale flow at the bottom of the inner layer. A major difference with the hydrostatic case though, is that all the upward gravity waves are reflected back toward the surface. The deceleration they produce in the far field in the hydrostatic case, generally referred to as the gravity wave drag, is now occurring in the upper part of the inner layer.

We showed in Part II that the transition from form drag to wave drag regimes occurs for values of the Richardson number $J \sim 1$. Indeed, the characteristic turning height of the waves is around $\sqrt{J}L$, such that wave dynamics can develop aloft and over the mountain when J is large, whereas it is somehow inhibited when J is small. Hence, we observed that when $J \approx 1$, the waves are reflected at altitudes about the length of the hill, and so, they are still close to the mountain when they return to the surface. It results destructive and constructive interactions between the wave induced pressure fields and the orography which produces low and high drag states, respectively.

However, a limitation of Part I and II is that we excluded trapped lee waves from our analysis. Indeed, trapped lee waves cannot develop in constant shear flow, in part because pure trapped modes are related to neutral modes of Kelvin-Helmholtz (KH) instability (Lott 2016; Soufflet et al. 2019), and so to emerge, such modes require that the Richardson number J varies in the vertical according to the Miles-Howard theorem (Miles 1961; Howard 1961). Trapped lee waves are important because they can transport momentum in the horizontal direction only (Bretherton 1969), and this horizontal transport can be as significant as the one due to upward propagating mountain waves (Teixeira et al. 2013). To reconcile such an horizontal transport of momentum and the non-interaction Eliassen-Palm non-interaction theorem (Eliassen and Palm 1961) one simply have to translate this momentum transfer into pseudo-momentum fluxes (Lott 1998; Georgelin and Lott 2001) (see also Broad (2002); Héreil and Stein (1999)).

Note that horizontal momentum transport by lee waves is still not well parameterized in coarse resolution models, even if Tsiringakis et al. (2017) showed that trapped lee waves could contribute as much as the blocked-flow drag (Lott and Miller 1997) or the turbulent orographic form drag (Beljaars et al. 2004), a conclusion also shared with observational studies (Steeneveld et al. 2009). Trapped lee waves could thus be a good candidate to account for the missing drag in the stable boundary layer (Sandu et al. 2019).

The purpose of the present paper (Part III) is to study the impact of trapped lee waves when they coexist with upward propagating waves by introducing a curvature in the background wind. Because boundary layer winds are generally small near the surface and present significant curvature near the top of the boundary layer, we will use this curvature to define a boundary layer height d (which should not be confused with δ, the inner layer scale over which waves are affected by dissipation). We will only consider boundary layers thicker than the inner layer ($d > \delta$). In this configuration, we will analyze how the boundary layer depth influences the transition between the form drag regime and the wave drag regime, and also how it impacts the Reynolds stress vertical profiles. We will also point out the role of trapped lee waves in this transition, and quantify their contribution to the wave drag.

The framework of this paper is close to the one used in L16. However, it is important to underline two major differences. First, in L16, the dynamics is inviscid and does not take into account the viscous dissipation in the boundary layer. Second, the influence of the boundary layer height (d) and the stability of the flow (J) will be here investigated independently which was not the case in L16 where the static stability was kept constant and the Richardson number was changed by varying the value of d.

The remainder of this paper is organized as follows. In section 1, we adapt the theoretical model from Part II to include an incident wind profile with a variable shear. In section 2 we study the impact of variable shear on the wave field and drags induced by the mountain. In section 3 we explain the onset of lee waves in the model and in section 4, we explain how they contribute to the interaction between the mountain and the large-scale flow. Last we analyze a pseudo-momentum budgets in section 5.

1. Theoretical framework

a. Linear model

The theoretical framework used here is close to the one used in Part I and II, so we only recall here the salient features and emphasize the differences. For instance, the background wind and density profiles are now given by,

$$u_0(z) = u_{0z} d \tanh(z/d), \;\; \rho_0(z) = \rho_r + \rho_{0z} z, \qquad (2)$$

where the surface wind shear u_{0z} and stratification ρ_{0z} are both constant. We choose this particular profile to represent the mean wind in the boundary layer because it is solution of the viscous equations near the surface but becomes constant above d, allowing a fraction of the mountain waves to propagate upward without being reflected. In the remainder of this analysis, we will refer to d as the boundary layer height. As we shall see, this wind profile supports the existence of pure trapped lee waves, at least when $J < 0.25$ and in the inviscid limit, a dynamic that was completely absent in Part I and II. Topography is still represented by a 2D Gaussian ridge of characteristic length L

$$h(x) = He^{-x^2/(2L^2)}. \qquad (3)$$

We also use the non-dimensional scaling of Part II,

$$(x,z) = L(\overline{x},\overline{z})\;;\;(u',w') = u_{0z}L(\overline{u},\overline{w})\;;$$
$$p' = \rho_r u_{0z}^2 L^2 \overline{p}\;;\; b' = u_{0z}^2 L\overline{b}, \qquad (4)$$

where the prime denotes eddy flow with respect to the background profile, and the overbars are used for non dimensional variables, x and z are the horizontal and vertical dimensions and u, w, p, and b are the horizontal and vertical velocity, the pressure and buoyancy respectively. With this scaling, the 2D Boussinesq linear equations, under the Prandlt approximation, are

$$\overline{u}_0\partial_{\overline{x}}\overline{u}+\overline{u}_{0\overline{z}}\overline{w}=-\partial_{\overline{x}}\overline{p}+\overline{\nu}\partial^2_{\overline{z}}\overline{u}, \tag{5a}$$

$$\overline{u}_0\partial_{\overline{x}}\overline{w}=-\partial_{\overline{z}}\overline{p}+\overline{b}+\overline{\nu}\partial^2_{\overline{z}}\overline{w}, \tag{5b}$$

$$\overline{u}_0\partial_{\overline{x}}\overline{b}+J\overline{w}=P^{-1}\overline{\nu}\partial^2_{\overline{z}}\overline{b}, \tag{5c}$$

$$\partial_{\overline{x}}\overline{u}+\partial_{\overline{z}}\overline{w}=0, \tag{5d}$$

in which

$$\overline{u}_0(\overline{z})=D\tanh(\overline{z}/D). \tag{6}$$

In that context no slip boundary conditions are

$$\overline{h}(\overline{x})+\overline{u}(\overline{x},\overline{h})=0,\ \ \overline{w}(\overline{x},\overline{h})=0,$$
$$\text{and }\ J\overline{h}(\overline{x})+\overline{b}(\overline{x},\overline{h})=0 \text{ at } \ \overline{h}=S\,e^{-\overline{x}^2/2}. \tag{7}$$

In Eqs. (5)-(7),

$$J=-\frac{g\rho_{0z}}{\rho_r u^2_{0z}},\ P=\frac{\nu}{\kappa},\ S=\frac{H}{L},\ D=\frac{d}{L}\ \text{ and }\ \overline{\nu}=\frac{\nu}{u_{oz}L^2} \tag{8}$$

are a Richardson number, a Prandtl number, a slope parameter, a non dimensional boundary layer depth, and an inverse Reynolds number respectively. With this new background flow profile the action budget is of form

$$\frac{\partial}{\partial\overline{x}}\underbrace{\left(\overline{u}_0\underbrace{\left(\frac{\overline{\zeta}\overline{b}}{J}-\frac{\overline{u}_{0\overline{z}\overline{z}}\overline{b}^2}{2J^2}\right)}_{A}+\frac{\overline{b}^2}{2J}+\frac{\overline{u}^2-\overline{w}^2}{2}\right)}_{F^x}+\frac{\partial}{\partial\overline{z}}\underbrace{(\overline{u}\overline{w})}_{F^z}=$$
$$\underbrace{\frac{\overline{\nu}}{J}\left(\overline{b}\partial^2_{\overline{z}}\overline{\zeta}+P^{-1}\partial^2_{\overline{z}}\overline{b}\left(\overline{\zeta}-\overline{b}\frac{\overline{u}_{0\overline{z}\overline{z}}}{J}\right)\right)}_{Q} \tag{9}$$

with $\overline{\zeta}=\partial_{\overline{z}}\overline{u}-\partial_{\overline{x}}\overline{w}$ the vorticity, A the pseudo-momentum, F^x, F^z, the horizontal and vertical fluxes of pseudo momentum, and Q the pseudo-momentum production/destruction by dissipative processes.

As in Part I (Eqs. 10 and 11), we search inflow solutions that are linear, and express them in Fourier space in the horizontal direction. For instance Eq. (5a) here transforms into

$$i\overline{k}\overline{u}_0\overline{\mathbf{u}}+\overline{u}_{0\overline{z}}\overline{\mathbf{w}}=-i\overline{k}\overline{\mathbf{p}}+\overline{\nu}\partial^2_{\overline{z}}\overline{\mathbf{u}}, \tag{10a}$$

where the bold notation is used for variables in the Fourier space.

For high Reynolds number $\overline{\nu}\ll 1$, the dynamics is inviscid at leading order. Each harmonics satisfy Eqs. (10) with $\overline{\nu}=0$, which results in $\overline{\mathbf{w}}$ satisfying a Taylor Goldstein equation of the form

$$\overline{\mathbf{w}}_{\overline{z}\overline{z}}+\left[\frac{J}{\overline{u}_0^2}+\frac{2}{D^2}\left(1-\frac{\overline{u}_0^2}{D^2}\right)-\overline{k}^2\right]\overline{\mathbf{w}}=0. \tag{11}$$

We find the solution of Eq. (11) using appropriate change of variables (see appendix A1 and Lott et al. (1992)) and we get

$$\overline{\mathbf{w}}_I=2^{-m}r^{\frac{1}{4}+i\frac{\mu}{2}}(1-r)^{-\frac{m}{2}}W_{2(1)}\underset{\overline{z}\to\infty}{\approx}e^{-m\overline{z}/D}, \tag{12}$$

where $r=\tanh^2(\overline{z}/D)$. In (12),

$$\mu=\sqrt{|J-\frac{1}{4}|},\ \text{and}\ m=\sqrt{|J-D^2k^2|}, \tag{13}$$

where m is the vertical wave number. Note that μ and m are changed in $i\mu$ and/or $-im$, when $J<1/4$ and/or $k^2D^2-J<0$, respectively. Note also that the hydrostatic approximation is simply derived by omitting the horizontal wavenumber $\overline{k}$ in Eqs. (11) and (13).

In Eq. (12), $W_{2(1)}$ can be expressed in terms of hypergeometric functions, and the solutions for $k<0$ are constructed by using the complex conjugate of the solutions with $k>0$. Near the surface the inviscid solution has an asymptotic behavior of the form,

$$\overline{\mathbf{w}}_I(\overline{k},\overline{z})\underset{\overline{z}\to 0}{\approx}\overline{\mathbf{w}}_M(\overline{k},\overline{z})=\overline{a}_1(\overline{k})\overline{z}^{1/2-i\mu}+\overline{a}_2(\overline{k})\overline{z}^{1/2+i\mu}, \tag{14}$$

where $\overline{\mathbf{w}}_M$ is a matching function and $\overline{a}_1(k)$, $\overline{a}_2(k)$ are coefficients given in appendix A1 (they are independent of $\overline{k}$ in the hydrostatic approximation).

The background wind profile near the surface being close to the one used in Part II, the treatment of the viscous solution in the boundary layer is done in a similar way: we define a non-dimensional inner layer depth

$$\overline{\delta}=\left(\frac{\overline{\nu}}{\overline{k}}\right)^{1/3} \tag{15}$$

which represents the scale over which waves are affected by dissipation. In this region, a viscous solution $\overline{\mathbf{w}}_V$ is derived numerically that satisfy the lower boundary condition Eqs. (7) and that matches $\overline{\mathbf{w}}_M$ when $\overline{z}/\overline{\delta}\to\infty$:

$$\overline{\mathbf{w}}_\nu(\overline{k},\overline{z}/\overline{\delta})\underset{\overline{z}/\overline{\delta}\to\infty}{\approx}f_{12}(\overline{k})\overline{\mathbf{w}}_M(\overline{k},\overline{z}/\overline{\delta}). \tag{16}$$

In (16) $f_{12}(\overline{k})$ are proportionality coefficients imposed by the lower boundary condition and that control the disturbance amplitude in the outer region. From these three solutions ($\overline{\mathbf{w}}_I$, $\overline{\mathbf{w}}_M$, $\overline{\mathbf{w}}_V$) we construct a uniform approximation for $\overline{\mathbf{w}}$,

$$\overline{\mathbf{w}}(\overline{k},\overline{z}) = f_{12}(\overline{k})\,[\overline{\mathbf{w}}_I(\overline{k},\overline{z}) - \overline{\mathbf{w}}_M(\overline{k},\overline{z})(\overline{k},\overline{z})] + \overline{\mathbf{w}}_V(\overline{k},\overline{z}), \tag{17}$$

with similar expressions for the horizontal wind, buoyancy and pressure.

b. Non linear model

As in Part I and II, we will compare the theoretical model against nonlinear simulations using the MITgcm model (Marshall et al. 1997). The configuration of the model is almost the same as in Part II: the few differences are as follow. The horizontal size of the domain is extended to 100 km and the total height of the domain is set to 50 km. This is a bigger domain than in Part II to allow lee waves to propagate downstream and avoid numerical instability. We initialize the model with the background flow and run it forward in time for 24h (until we reach a steady state) with a time step of 0.2 s. We use a sponge layer active above 15 km and at the lateral boundaries to relax the dynamic variables to the prescribed upstream profiles (Eq. 2). We use a stretched grid to have maximum resolution near the topography. The finest grid point has dimension of 205 m (horizontal) and 11 m (vertical) near the topography whereas the resolution coarsen to 715 m (horizontal) and 830 m (vertical) at the edge of the domain.

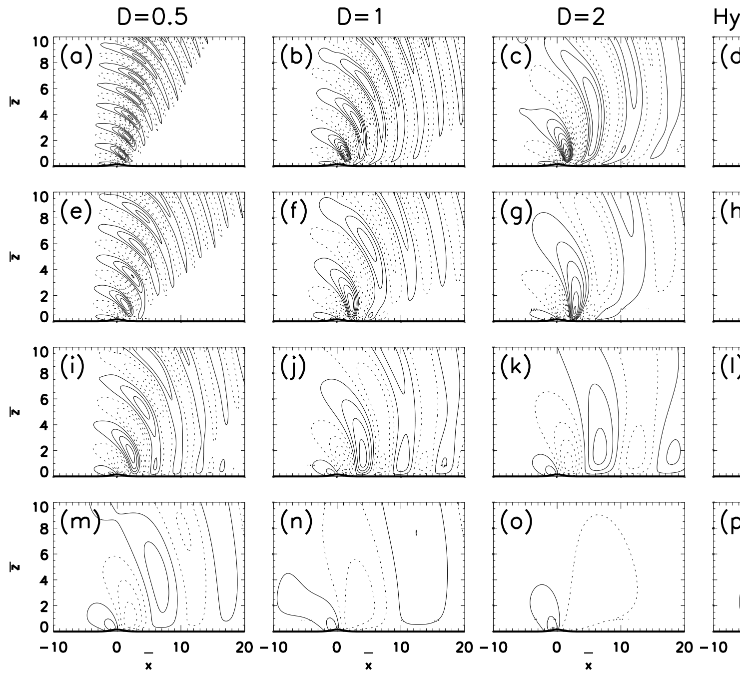

FIG. 1. Vertical velocity field for all simulation, $S = 0.15$. Each line corresponds to a value of J. The 3 columns on the left stand for different values of D and the column on the right is for the hydrostatic case with $D = 1$. In all panels, the contour interval $CI = 0.004$ and the negative values are dashed.

2. Upper level and trapped waves

We plot in Fig. 1 the vertical velocity field for different values of the boundary layer depth D and of the surface Richardson number J. In each simulations $S = 0.15$, $Pr = 2$ and the height of the inner layer for the dominant harmonic $\overline{k} = 1$ is $\overline{\delta} = 0.1$. We also plot the hydrostatic results for $D = 1$ to emphasize the significance of the reflected waves and of the trapped lee waves.

The top four panels in Fig. 1 show the vertical velocities in the stratified case ($J = 4$). We choose to present the $J = 4$ case first because it corresponds to the first figures shown in Part I and II, e.g. the hydrostatic case with constant shear in Part I (Fig. 1) and the non-hydrostatic case with constant shear in Part II (Fig.1). For the smallest value $D = 0.5$, Fig. 1a shows a train of upward propagating waves with a small downstream signal at low level. At upper levels the wave field extends downstream in comparison with the hydrostatic case (Fig. 1d) indicating that non-hydrostatic effects essentially make a difference at high altitudes. To understand why the low level signal is small in this case, we recall that the square of the vertical wavenumber is given by (see Eq. (13)),

$$\overline{m}^2 = J - D^2\overline{k}^2. \tag{18}$$

So the only modes that encounter a turning altitude are those for which $\overline{k} > \sqrt{J}/D$. In Fig. 1a the shape of the mountain will force the dominant wavenumber to be $\overline{k} \approx 1$, and for $\overline{k} > \sqrt{J}/D = 4$, most modes will not be reflected. As D increases nevertheless the amount of reflected waves increases (Fig. 1b and 1c) and the wave signal near the surface becomes more pronounced downstream. An interesting aspect is that when these waves return to the surface on the lee side, their phase lines tilt significantly in the direction of the shear. This is consistent with the fact that for large J, the mountain waves are absorbed at the surface in the stable cases (Lott (2007)): the signal is dominated by downward propagating waves being absorbed.

The following two rows in Fig. 1 correspond to the two values of the surface Richardson number that characterized the best the transition between the stratified and neutral case in Part II (i.e. when $D = \infty$). At $J = 1.7$ we found in Part II that there is a resonant interaction between reflected waves and the surface that yields a very strong wave signal aloft and immediately downstream, whereas for $J = 0.7$, we found that the interaction is destructive and the disturbance field is evanescent. The fact that waves can now propagate upward to $z = \infty$ when D is finite profoundly changes the response. The cases with $J = 1.7$ (second row in Fig. 1) are close from the cases with $J = 4$ except that the

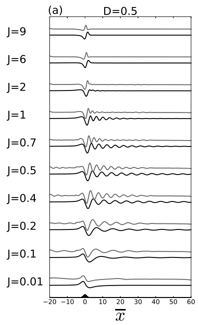

FIG. 2. Horizontal profiles of vertical velocity at $\overline{z} = D$ for $S = 0.15$. Each panel corresponds to a value of D and each line to a value of J. Profiles from the MITgcm model are represented in grey.

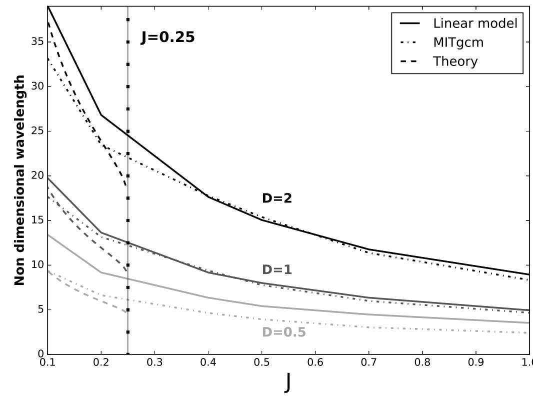

FIG. 3. Lee waves wavelength function of stability calculated from Eq. (19) (dashed), linear model (solid) and MITgcm model (dash-dotted). Each grey scale stand for a different value of D.

overall direction of propagation is more horizontal, consistent with the fact that far aloft more modes are impacted by non-hydrostatic effects. When $J = 0.7$ (third row in Fig. 1), we still visualize a system of gravity waves, which was not the case in Part II (Fig. 3c). Most gravity waves are propagating up when $D = 0.5$ (Fig. 1i) but there is now a system of downstream and horizontally propagating waves near the surface. For these waves, the phase line are more vertical, indicative of a smaller wave absorption at the surface, the signature is very much like that of a trapped lee wave. When D increases (Figs. 1j and 1k) these near surface waves become more and more prominent, which is again consistent with the fact that less modes can propagate far aloft according to (18). Interestingly, when D increases, the horizontal wavelength near the surface increases as well. Finally, for $J = 0.1$ (Figs. 1m-p), there are few upward waves: the near surface signal dominates but remains overall small.

3. Lee waves

As shown in Figure 1, a significant difference between Part I-II and this study is the presence of trapped lee waves for small values of the Richardson number J. In this section we analyze the impact of the boundary layer height D and stability J on the onset of these trapped lee waves and compare the results with the non-linear model (MITgcm).

We plot in Fig. 2 the horizontal profiles of vertical velocity at $\overline{z} = D$ for $S = 0.15$ in the theory (black) and in the MITgcm (grey). Each panel corresponds to a different value of D, and J is decreasing from top to bottom. In Fig. 2, we see that weakly stratified flows ($J < 1$) favor the onset of trapped lee waves regardless of the value of D, due to weaker wave absorption at the ground. This result extends the quasi-inviscid theoretical framework of L16 who showed that near-surface critical level absorption is an active dissipation process. Hence, in the present study, the same mechanism is still at play even when viscous dissipation acts in the inner layer near the ground. Note also that, due to dissipation, the downstream extent of lee waves is reduced compared to the quasi-inviscid results in L16 (even for $J < 0.25$).

We also observe that the trapped lee wave signal is small when J is small (for instance when $J = 0.01$ and $J = 0.1$). This is actually in agreement with L16 who showed that the trapped lee waves are also near neutral modes of KH instability. Hence for the vertical profile of horizontal wind given in (6), these modes satisfy the dispersion relation:

$$\overline{k}_T^2 = \frac{1 - \sqrt{1 - 4J}}{2D^2} \quad \text{when} \quad J < 1/4. \tag{19}$$

It follows that for near-neutral flow ($J \ll 1$), and for $D \gtrsim 1$, the trapped lee waves have predominant wavelength $\overline{k}_T \ll 1$. Such wavelength correspond to quite long disturbances which are not efficiently excited when the orography has a Gaussian shape. For such a shape the non-dimensional wavenumbers excited by the mountains are predominantly around $\overline{k} \approx 1 \gg \overline{k}_T$.

To support this interpretation, we plot in Fig. 3 the lee waves wavelength for different value of J and D as calculated with the dispersion relation (19), the theoretical model and the MITgcm. One sees a good agreement between the different sources (compare each line style of the same color). We also see that the increase in boundary layer height systematically increases the lee waves wavelength whereas the increase in stability tends to reduce it, which is entirely consistent with (19). The theoretical model (solid line) slightly overestimates the wavelength for small values of D. This difference might be because as the value of D decreases, the domain of validity of the inner and inviscid solution overlapped, then the validity of the uniform approximation could be questioned. This also explains why we limit our study to $D \geq 0.5$. The above

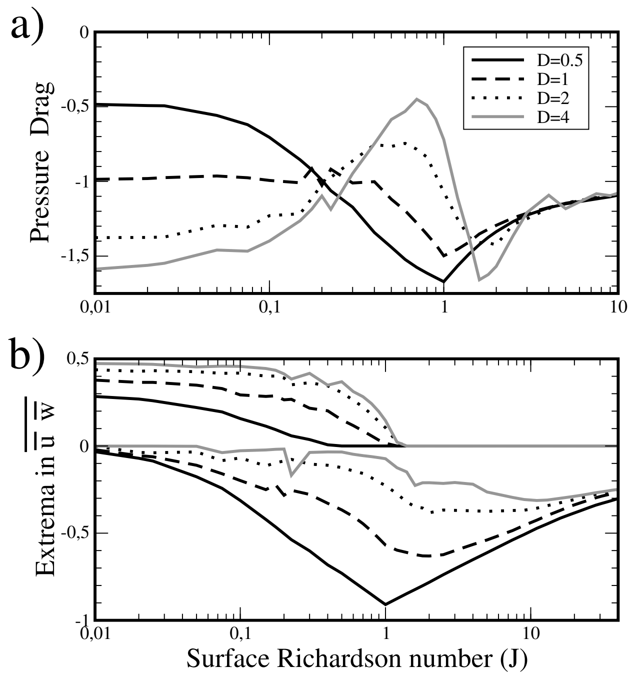

FIG. 4. Surface pressure drag (a) and minimum and maximum of Reynolds stress (b) for different slope S and $D = 1$ in variable shear simulations. These two diagnostics are normalized by D_{r_P} (Eq. (21)).

results corroborate the observational study of Ralph et al. (1997) where the increase of boundary layer height during daytime induces an increase of lee waves wavelength.

If we now return to Fig. 2, another interesting point is that low level oscillations can be found when D and J are large (see for instance Figs. 2c for $J = 6$ and $J = 9$). This can also be explained with Eq. (18), which tells that when J and D are large some modes with $\overline{k} \approx 1$ can be reflected back to the surface. However, since this reflection occurs at high altitude (D is large), they return to the surface further downstream (we already noticed that in Figs. 1b and 1c). In this case the lee waves signal near the surface results from waves reflected downward in the lee side (referred as trapped waves or reflected waves in the remainder of this analysis) and do not correspond to trapped *lee* waves in the sense that they are not related to free modes of oscillation that exist in the inviscid case.

4. Pressure drag and Reynolds stress

To evaluate the effects of the wave field on the mean flow, we plot in Figs 4a and 4b the surface pressure drag Dr along with the minimum and maximum of the mountain wave stress $\overline{F}^z$:

$$Dr = -\int_{-\infty}^{+\infty} \overline{p}(\overline{x}, \overline{h}) \frac{\partial \overline{h}}{\partial \overline{x}} d\overline{x}, \qquad \overline{\overline{u\,w}} = \overline{F^z} = \int_{-\infty}^{+\infty} \overline{u}\,\overline{w}\, d\overline{x}. \tag{20}$$

These diagnostics are scaled using the drag predictor derived in Part II

$$D_{r_P} = \mathrm{Max}(1, \sqrt{J})\overline{\delta}(1) S^2/2. \tag{21}$$

We recall that the idea behind this formulation is to scale mountain drag as a form drag in weakly stratified cases ($J < 1$) due to dissipative loss of pressure when the air passes over the obstacle, and as a wave drag, when the flow is more stratified ($J > 1$), due to vertical propagation of gravity waves.

In Fig. 4a, we see that the drag predictor gives a rather good estimate of the surface pressure drag in a large range of flow stability J and boundary layer depth D. The best performance of the predictor is for $D = 1$, (black dashed line). For smaller value (for instance $D = 0.5$) the form drag predictor overestimates the drag when $J < 0.1$. This is consistent with the fact that for small D, only few harmonics are confined near the surface. So for small D, these "long" harmonics contribute less to the near surface dynamics responsible of the form drag than for larger D. When $D > 1$, we recover the behavior found in Part II where the transition zone around $J = 1$ present strong variations in pressure drag. For instance, for $D = 4$ in Fig. 4a we recover the behavior found in Fig. 2 of Part II ($D = \infty$), with a pronounced low drag amplitude near $J = 0.7$ and a large drag amplitude near $J = 1.7$.

Interestingly, the transition from neutral to stratified flow when D is large occurs more smoothly when $D \approx 1$ (less amplitude between the lowest and highest value of the drag during the transition). To understand this behavior, we recall again that the mechanism which causes the strong variations in drag when D is large is due to the fact that most harmonics are reflected and return to the surface near the mountain downstream when $J \approx 1$. In the variable shear case, the dominant wave numbers are no longer systematically trapped, for instance the dominant one $\overline{k} = 1$ is only trapped when $J/D^2 < 1$. For instance, when $J \ll 1$ this only occurs when D is small, e.g. when gravity waves no longer control the dynamics.

Figure 4b shows the minimum and maximum of horizontally averaged Reynolds stress $\overline{\overline{u\,w}}$ (normalized by the predictor). These normalized extrema indicate how the wave field interacts with the mean flow. When the vertical profile of Reynolds stress presents a minimum at a given height, the mean flow is accelerated below that height, and decelerated above (the so-called gravity wave drag) and this situation corresponds to a wave drag regime. On the contrary, when the vertical profile of Reynolds stress is maximum at a given height, the mean flow is decelerated

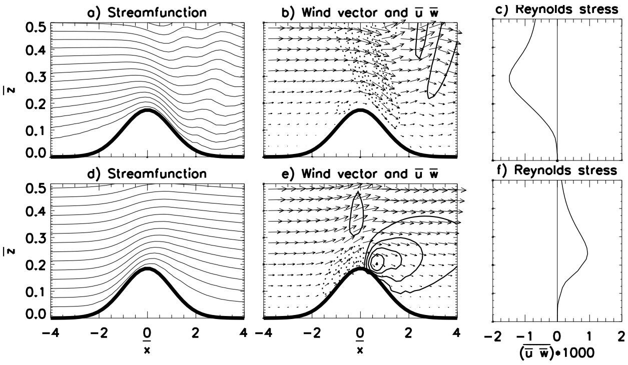

FIG. 5. Stream function (a,d), total wind vector and contours of $\overline{u}\,\overline{w}$ (negative values are dashed) (b,e) and profiles of horizontally averaged Reynolds stress $\overline{\overline{u}\,\overline{w}}$, $S = 0.175$, $D = 4$. Top panels correspond to $J = 9$, bottom panels to $J = 0.1$.

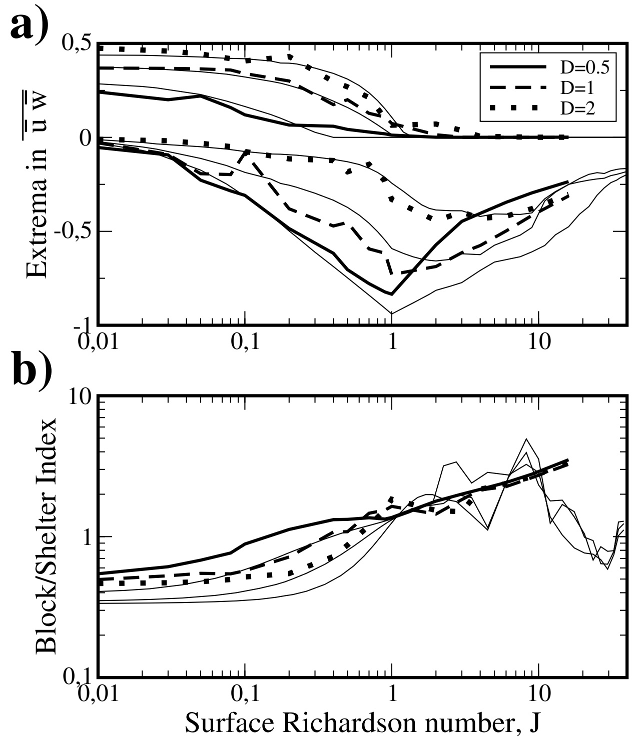

FIG. 6. Diagnostics from the MITgcm runs for $S = 0.15$ and for different values of the boundary layer depths D. In all panels, the corresponding results from the theory are in thin solid. a) Normalized extrema in momentum flux . b) Downslope sheltering versus upstream blocking index defined as the ratio between the max downslope wind amplitude and the max upslope wind amplitude (Eq. 28 from Part II):

$$\underbrace{\mathrm{Max}}_{\overline{z}<\frac{2\overline{h}}{3},0<\overline{x}<2} \sqrt{(\overline{z}+\overline{u})^2+\overline{w}^2} \Bigg/ \underbrace{\mathrm{Max}}_{\overline{z}<\frac{2\overline{h}}{3},-2<\overline{x}<0} \sqrt{(\overline{z}+\overline{u})^2+\overline{w}^2}\ .$$

below that height, this situation corresponds to a form drag regime. Before discussing these regimes in detail, it is worth recalling that these changes in sign of the Reynolds stress have a profound dynamical origin. To illustrate it qualitatively, we show in Fig. 5 two cases with $D = 4$ and $S = 0.175$ (strong slope). In the first case, the flow is strongly stratified ($J = 9$) and is characterized by upstream blocking and downslope winds (Figs. 5a and 5b respectively). In the downslope wind region where $\overline{w} < 0$ the disturbance in horizontal wind $\overline{u} > 0$, yielding the product $\overline{uw} < 0$ predominantly (see contours in Fig. 5b). Averaged horizontally, this gives a negative Reynolds stress (Fig. 5c). In the second case shown in Fig. 5, the flow is near neutral ($J = 0.1$) the dynamics is characterized by upslope winds upstream and non separated sheltering downstream as illustrated by the stream function and the wind fields in Figs. 5d,e. But in the sheltered zone the horizontal wind is smaller, so the disturbance wind $\overline{u} < 0$ predominantly. Because this zone is located on the lee of the mountain the vertical velocity $\overline{w} < 0$ predominantly, so the product $F^z = \overline{uw} > 0$ as shown in a large sector behind the hill top in Fig. 5b. Averaged horizontally, this yields a positive Reynolds stress (see Fig. 5c).

If we now return to the extrema in $\overline{\overline{F^z}}$ in Fig. 4b, one sees that positive and negative extrema can occur simultaneously in the near neutral cases ($J < 1$), at least when $D \leq 1$. This strongly contrast with what was found in Part II (or for $D = 4$ here) where form drag and wave drag do not occur simultaneously. For values of $D < 4$, one sees that form drag and wave drag are no longer exclusive of each other, clearly here the presence of trapped waves and the fact that more waves can propagate aloft when D is small extent the domain over which the gravity waves dynamics contribute to the interaction between the orography and the large scale flow. In Fig. 4b we also see that positive extrema only occur for $J < 0.4$ when $D = 0.5$, which means that in the presence of a thinner boundary layer the transition from neutral to stratified flow occurs for smaller values of the surface Richardson number J.

To assess the validity of this result, we now compare the linear model with the fully non-linear model (MITgcm). For conciseness, we summarize this comparison in Fig. 6 using again the diagnostics of the extrema of the Reynolds stress (Fig. 6a), and also the index constructed in Part II (see Eq. 28 there): we recall that this index discriminates between the regime of downslope sheltering vs the regime of upstream blocking. Since the results for $D = 4$ correspond to $D = \infty$ in Part II, we only present the aforementioned diagnostics for $D = 0.5, 1, 2$. For all these indicators, we see that the non-linear model is in good agreement with the linear theory. Last we also observe that the sheltering versus blocking index introduced seem to not depend on the value of D.

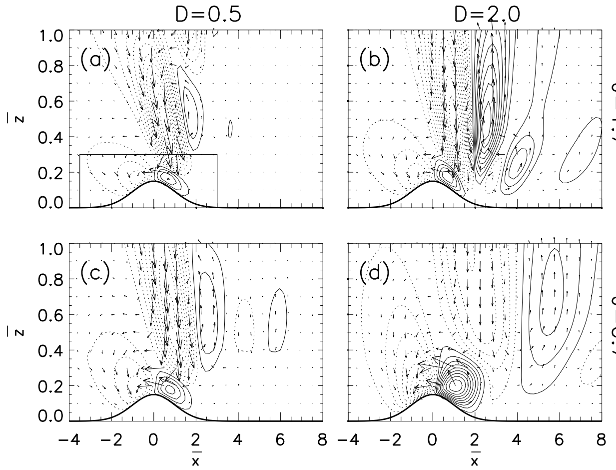

FIG. 7. Contours of vertical action component ($F^{\overline{z}}$), negative values are dashed, along with total action vector for $S = 0.15$. For illustration in a) are the limit of a characteristic box used to calculate the emitted PM fluxes.

5. Pseudomomentum budget

We have shown that in the presence of an inner layer and a boundary layer, form drag and wave drag coexist, which then directly impact the structure of the vertical profile of the Reynolds stress. We have also seen that the presence of a finite boundary layer depth enriches the inviscid dynamics, with trapped waves developing downstream the topography. We now provide more insight on the way these waves redistribute momentum not only in the vertical but also in the horizontal direction. To visualize this redistribution of momentum, we plot in Figure 7 contours of vertical the flux of action component (F^z defined in Eq (9)) along with the total action flux vector for different value of the Richardson number J and boundary layer depth D.

In all panels in Fig. 7 one sees near the ground a downward flux on the upstream side of the ridge (dashed lines) and an upward flux on the downstream side (solid lines). This dipole structure in the lower part of the inner layer is characteristic of the dynamics at work in our three part paper and that we could refer to as linear dissipative, or weakly nonlinear dissipative. The key point is that when the mountain is in the inner layer, waves pseudo-momentum is extracted from the inner layer rather from the surface as it occurs in the inviscid case. Near the top of the inner layer (i.e. around $\overline{z} = 5\overline{\delta}$) and above, one sees in Fig. 7a that for small D and $J = 1.7$ the pseudo-momentum flux vector points downward, as in the hydrostatic case in Part I, such that the trapped waves (present for instance in Figs. 1e and to less extent in Fig 2a) contribute little to the action flux. For larger D in Fig. 7b the reflected waves downstream produce an upward pseudo-momentum flux, also slightly oriented upwind on the lee side, as if the trapped waves where transferring momentum laterally rather than vertically. This larger contribution of the trapped waves to the pseudo-momentum budget is consistent with the fact that for $J = 1.7$ and $D = 2$ in Fig. 1g the low level wave signal is quite substantial. For smaller J (Figs. 7c and 7d), the trapped lee waves seem to contribute further in the far field, at least when $J = 0.7$, consistent with the fact that for small J, the mountain waves are less absorbed at the surface.

To provide a more quantitative estimate of the lateral fluxes due to the reflected and/or the trapped lee waves we next evaluate pseudo-momentum fluxes through horizontal and vertical boundaries that encapsulate well the entire ridge. More specifically, we calculate the pseudo momentum fluxes outgoing from the top hat defined by the three segments.

$$(-\overline{X},0)\times(-\overline{X},\overline{Z}),\ (-\overline{X},\overline{Z})\times(+\overline{X},\overline{Z}),\ (+\overline{X},\overline{Z})\times(+\overline{X},0) \tag{22}$$

and always take $\overline{Z} > \overline{h}$ and $\overline{X} > 3$, the latter condition guaranties that $\overline{h}(\pm\overline{X}) \approx 0$. The integral of the pseudo momentum fluxes across the boundaries writes

$$P^x(\overline{X},\overline{Z}) = \int_0^{\overline{Z}} F^x(\overline{X},\overline{z})d\overline{z} \text{ and } P^z(\overline{X},\overline{Z}) = \int_{-\overline{X}}^{\overline{X}} F^z(\overline{x},\overline{Z})d\overline{x}. \tag{23}$$

$$P^{\text{out}}(\overline{X},\overline{Z}) = P^x(\overline{X},\overline{Z}) - P^x(-\overline{X},\overline{Z}) + P^z(\overline{X},\overline{Z}). \tag{24}$$

As the in-going flux is always quite small, we will only discuss the fluxes along the upper and downstream sides of the box. The solid lines in Fig. 8 are the vertical profiles of the total outgoing momentum fluxes, $P^x(\overline{X},\overline{Z}) + P^z(\overline{X},\overline{Z})$ for 3 different downstream locations: one near the mountain $\overline{X} = 3$ one further downstream $\overline{X} = 5$, and one very far downstream $\overline{X} = 25$. We selected the first two positions to illustrate the large erosion of the emitted pseudo momentum fluxes (P^{out}) that occur just downstream the hill (i.e. between $\overline{X} = 3$ and $\overline{X} = 5$). And we selected $\overline{X} = 25$ to measure the total erosion occurring in the boundary layer (in $\overline{X} = 25$ we found that the lateral pseudo-momentum flux is almost always null, see the thick grey dotted lines in Fig. 8). The first thing to notice is that for all values of D and J, the total flux of pseudo momentum $P^{\text{out}}(\overline{X},\overline{Z}) = const.$ on the vertical when $\overline{Z} > 5\overline{\delta}$, i.e. when the upper bound $\overline{Z}$ is in the inviscid region. This can be viewed as a generalization of the Eliassen-Palm theorem in the presence of trapped lee waves. Also, and when D is small ($D = 0.5$ in Figs.8a,c), almost all the pseudo-momentum flux is transmitted vertically through the boundary layer: the lateral fluxes of pseudo-momentum are always small, at least below $\overline{Z} = D$ (see the dotted lines). Above the boundary layer, the lateral propagation of the gravity waves in the inviscid region produces substantial horizontal fluxes when the downstream distance is not too large ($\overline{X} = 3$ and $\overline{X} = 5$, thick and thin dotted black lines respectively, see also Fig. 1). When

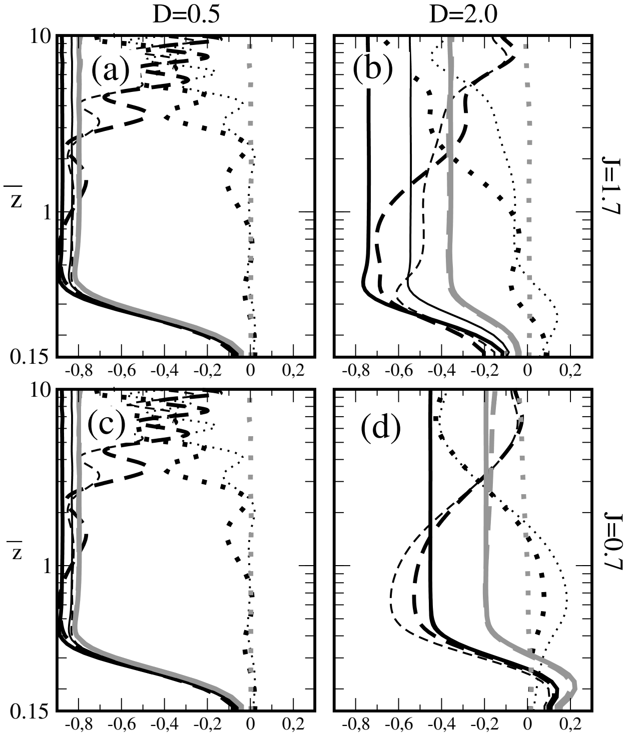

Fig. 8. Vertical profile of P^z (dashed), P^x (dot) and the sum (P^{out}, solid) for different downstream position: $\overline{X} = 3$ (thick black); $\overline{X} = 5$ (thin black); and $\overline{X} = 25$ (thick grey).

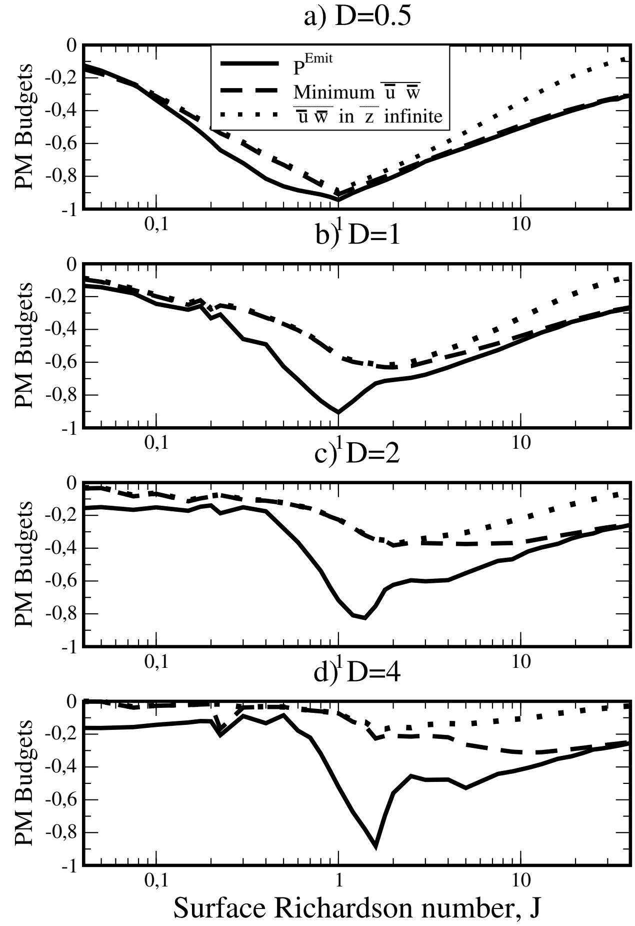

Fig. 9. Emitted pseudo momentum, minimum and emitted value of the Reynolds stress. In all simulations $S = 0.15$.

$D = 2$ in Figs. 8b one sees that the total pseudo-momentum fluxes diminishes in amplitude when $\overline{X}$ increases and in the inviscid zone $\overline{Z} > 5\overline{\delta} = 0.5$. This diminution is due to the fact that for large values of D, there are more reflected waves returning into the inner layer than when D is smaller. Moreover, these reflected waves are associated with positive vertical fluxes of pseudo-momentum $F^{\overline{z}}$. Therefore when the horizontal extension of the upper bound of the box increases, these reflected waves cancel the negative contribution of the upward waves in the integral flux P^z. This mechanism combines with a substantial contribution of the trapped lee waves propagating horizontally and at lower level when $J = 0.7$ in Fig. 8d. In this case one sees that the amplitude of the vertical flux first increase between $5\overline{\delta} < \overline{Z} < D$ (above the inner layer but inside the boundary layer) when $\overline{X}$ increases consistent with the fact that the reflected waves are less absorbed when J decreases.

As seen in Part I and II, and repeated here, it is quite difficult to pin the location of extraction of pseudo-momentum. It is not entirely extracted from the surface and equals to the pressure drag as in the inviscid case (Durran 1995; Lott 1998), and it is not extracted from the viscous fluid in the inner layer as in the case with $S \ll \overline{\delta}$ (Part I). Because of these difficulties, we instead propose to diagnose the largest amount of pseudo momentum that is produced by the association between the mountain and the inner layer. We next call it the emitted pseudo-momentum, and evaluate it as the total pseudo-momentum flux going out of the top hat defined by (22) with lateral boundary near the downstream foot of the hill $\overline{X} = 3$ and upper boundary at the altitude Z_T that minimises the outgoing flux:

$$P^{\mathrm{Emit}} = P^x(3, \overline{Z}_T) + P^z(3, \overline{Z}_T) = \min_{S<\overline{Z}<\infty} \left(P^x(3, \overline{Z}) + P^z(3, \overline{Z}) \right). \tag{25}$$

A typical box through which is measured the emitted PM flux is shown in Fig. 7a for illustration. To measure how much of this emitted flux goes in gravity wave drag far aloft and to estimate what stays at low level, we compare P^{Emit} to the far field Reynolds stress, and to the minimum in Reynolds stress,

$$\overline{F^z}(\overline{Z} = \infty), \text{ and } \min_{S<\overline{Z}<\infty} \overline{F^z}, \tag{26}$$

respectively. As we defined the Reynolds stress using the vertical component of action $F^{\overline{z}}$ (see (Eq. 9)), and because its minimum is always found well inside the inner layer, we can conservatively consider the difference between the emitted pseudo-momentum flux and the minimum in Reynolds stress as the part due to horizontal propagation yielding to wave large-scale flow interactions occurring inside the inner layer and downstream exclusively. Fig. 9 shows that when D increases the emitted pseudo-momentum fluxes and the minimum in Reynolds stress are quite different. More specifically, we find that for narrow boundary layers ($D = 0.5$ in Fig. 9a) lateral fluxes are small. We note also that the minimum in Reynolds stress is larger than the far field Reynolds stress when $J > 1$, the upward propagating waves are dissipated in the upper part of the inner layer (see also Part I). This effect occurs for all boundary layer depth D and is never pronounced for small J, as indicates the fact that the far field and minimum Reynolds stress always coincide for $J < 1$. As D increases up to $D = 1$ and for moderate stability $0.1 < J < 1$, the presence of lee waves induces a lateral flux, the emitted fluw P^{Emit} substantially exceeding the Reynolds stresses Fig. 9b. This lateral contribution decreases as J increases, the waves being absorbed at the surface. For larger D in Fig. 9c,d, the contributions of the lateral fluxes become more and more substantial, and for large J a good part of the lateral fluxes are due to the fraction of the emitted waves which are reflected downward (the surface absorption being large).

6. Conclusion

In this paper we have analyzed how a background wind curvature, which mimics a boundary layer of depth D, modulates the impact of small-scale mountains on the large-scale flow while staying in the weakly nonlinear dissipative regime used in Part I and II. The first noticeable result we find is that trapped lee waves develop much more than in the constant shear case, they resemble to Kelvin-Helmholtz neutral modes of instability, at least when the surface Richardson number $J < 0.25$. This corroborates the results in Lott (2016); Soufflet et al. (2019) but using an other boundary layer parameterization and an other fully nonlinear model (the MITgcm here versus WRF in Soufflet et al. (2019)). We also found that for large J and D, low level waves are related to modes that have been reflected at turning levels and that return to the surface downstream where they are absorbed. For small J, the trapped lee waves may not be efficiently excited, simply because the corresponding neutral modes of KH instability have small horizontal wavenumber compared to the characteristic scale of the mountain (a condition that writes $\overline{k} \ll 1$ in dimensionless form).

As in the constant wind shear cases we recover the transition from the form drag regime to the wave drag regime when the flow stability near the surface increases. The wave drag regime is associated with downslope winds and upstream blocking and is characterized by a negative Reynolds stress a good fraction of which radiates in the far field (see Fig. 5a,b,c). The form drag regime is associated with upslope winds and downstream sheltering and is always associated with positive Reynolds stress, confined to the inner layer (see Fig. 5d)e,f). One key result of this part is that there exists a transition zone for which these two regimes coexist. For this intermediate situations, the Reynolds stress is positive in the lower part of the inner layer and negative in the upper part and aloft: the interaction between the boundary layer flow and the mountain produces deceleration near the surface, acceleration in the middle of the inner layer, and deceleration (gravity wave drag) near the top of the inner layer and above. As a direct consequence, we can measure the relative importance of the form drag regime and of the wave drag regime by comparing the minima and maxima of the Reynolds stress.

The nature of this transition is controlled by the amount of reflected waves that return to the surface and by the absorptive properties of the surface. In this paper, we controlled the reflected waves with the boundary layer depth D, while we controlled the absorption with the surface Richardson number J. When D is small, most harmonics are free to propagate in the far field, upward propagating gravity waves control the dynamics for values of $J > 0.1$. When D increases the background wind curvature starts supporting horizontally propagating trapped lee waves when $J \approx 1$. For larger values of J, these trapped lee waves do not develop well (the ground absorption is too large) but, there can be vertically propagating waves returning from the far field to the surface where they are absorbed. We showed that, when they exist, trapped lee waves and reflected waves can produce significant lateral fluxes of momentum downstream the mountain. Pseudo momentum budget near the topography indicates that lateral and vertical momentum flux are of the same order of magnitude for intermediate values of J. These downstream fluxes remain substantial up to five time the mountain width, the associated lee wave drag being applied in the inner layer.

For future work, we wish to use our results to parameterize low-level drag in coarse resolution models. Indeed, we have a predictor (Eq. 21) and indications of where that the drag should be deposited. Compared to the results of Part II, we now know that the fraction of the drag due to trapped waves (those encountering turning levels in the low troposphere) should entirely be deposited at low level, where the waves are dissipated. We should also start discussing how form drag and wave drag should interact for these waves, since we just showed that they can coexist. Our results suggest that there exist a criteria to separate the harmonics that contribute to form and wave drag. Of course this criteria should be a function of the altitude of the turning levels and presumably also be a function of the boundary layer depth, not just the inner layer depth.

APPENDIX

A1. Calculation of the Outer solution

If we change variables and take $r = \tanh^2(\overline{z}/D)$ equation Eq. (11) transforms into:

$$\frac{d^2\overline{\mathbf{w}}}{dr^2} + \left(\frac{1}{2r} - \frac{1}{1-r}\right)\frac{d\overline{\mathbf{w}}}{dr} + \left(\frac{J}{4r^2(1-r)^2} + \frac{1}{2r(1-r)} - \frac{D^2\overline{k}^2}{4r(1-r)^2}\right)\overline{\mathbf{w}} = 0. \quad \text{(A1)}$$

This equation has three regular singular points in $r = 0, 1, \infty$, when $k^2D^2 - J > 0$ and $J > 1/4$ their exponent pairs are:

$$\begin{aligned} r = 0: &\quad \alpha_1 = \tfrac{1}{4} + i\tfrac{\mu}{2}, \quad \alpha_2 = \frac{1}{4} - i\frac{\mu}{2};\\ r = 1: &\quad \gamma_1 = -\tfrac{m}{2}, \quad \gamma_2 = +\frac{m}{2} \\ r = \infty &\quad \beta_1 = 1, \quad \beta_2 = -\frac{1}{2}. \end{aligned} \quad \text{(A2)}$$

In (A2),

$$\mu = \sqrt{|J - \frac{1}{4}|}, \text{and } m = \sqrt{|J - D^2k^2|}, \quad \text{(A3)}$$

they are changed in $i\mu$ and/or $-im$, when $J < 1/4$ and/or $k^2D^2 - J < 0$, respectively. Introducing the change of variable,

$$\overline{\mathbf{w}} = r^{\alpha_1}(1-r)^{\gamma_1}W \quad \text{(A4)}$$

equation (A1) transforms into the hyper-geometric equation, and the inviscid solution

$$\overline{\mathbf{w}}_I = 2^{-m} r^{\frac{1}{4}+i\frac{\mu}{2}}(1-r)^{-\frac{m}{2}}W_{2(1)} \underbrace{\approx}_{\overline{z}\to+\infty} e^{-m\overline{z}/D}, \quad \text{(A5)}$$

behaves like a pure exponential function in the far field, for instance like a unit amplitude upward propagating gravity wave when $D^2\overline{k}^2 < J$. In (A5), the solution

$$W_{2(1)} = (1-r)^m F(c-b, c-a; c-a-b+1; 1-r), \quad \text{(A6)}$$

is expressed using the hyper-geometric function F, and the coefficients

$$\begin{aligned} a = \alpha_1 + \beta_1 + \gamma_1 &= \frac{5}{4} + i\frac{\mu}{2} - \frac{m}{2},\\ b = \alpha_1 + \beta_2 + \gamma_1 &= -\frac{1}{4} + i\frac{\mu}{2} - \frac{m}{2},\\ c = 1 + \alpha_1 - \alpha_2 &= 1 + i\mu. \end{aligned} \quad \text{(A7)}$$

To evaluate $\hat{w}_c$ near the surface, the transformation (15.3.6 in AS) is used to express (A5) in terms of the solutions (15.5.3 in AS) and (15.5.4 in AS), e.g.

$$W_{1(0)} = F(a, b; c; r)\text{, and } W_{2(0)} = r^{1-c}F(a-c+1, b-c+1; 2-c; r): \quad \text{(A8)}$$

$$W_{1(0)} = A_1W_{1(1)} + A_3W_{2(1)},\ W_{2(0)} = A_2W_{1(1)} + A_4W_{2(1)} \quad \text{(A9)}$$

where

$$A_1 = \frac{\Gamma(c)\Gamma(c-a-b)}{\Gamma(c-a)\Gamma(c-b)}, \quad A_3 = \frac{\Gamma(c)\Gamma(a+b-c)}{\Gamma(a)\Gamma(b)},$$

$$A_2 = \frac{\Gamma(2-c)\Gamma(c-a-b)}{\Gamma(1-a)\Gamma(1-b)}, \quad A_4 = \frac{\Gamma(2-c)\Gamma(a+b-c)}{\Gamma(a-c+1)\Gamma(b-c+1)}.$$

This yields

$$\overline{\mathbf{w}}_I = r^{\alpha_1}(1-r)^{\gamma_1}\left(b_1W_{2(0)} + b_2W_{1(0)}\right),$$

$$\text{where } b_j = (-1)^{j-1}\frac{2^{-m}A_j}{A_1A_4 - A_2A_3} \text{ for } j = 1, 2. \quad \text{(A10)}$$

When approaching the surface, this inviscid solutions behaves as the matching function,

$$\overline{\mathbf{w}}_I(\overline{k}, \overline{z}) \underset{\overline{z}\to 0}{\approx} \overline{\mathbf{w}}_M(\overline{k}, \overline{z}) = \overline{a}_1(\overline{k})\overline{z}^{1/2-i\mu} + \overline{a}_2(\overline{k})\overline{z}^{1/2+i\mu}, \quad \text{(A11)}$$

providing that

$$\overline{a}_1 = D^{-\frac{1}{2}+i\mu}b_1, \text{ and } \overline{a}_2 = D^{-\frac{1}{2}-i\mu}b_2. \quad \text{(A12)}$$

Acknowledgement

This work was supported by the Laboratoire de Recherche Conventionné “Yves Rocard”, a collaborative unit between CEA and Ecole Normale Supérieure. The MITgcm used in the present study can be dowloaded at "mitgcm.org". The theoretical model is written in fortran, is available on F. Lott webpage: "www.lmd.jussieu.fr/ flott/homepage.html".

References

Beljaars, A. C. M., A. R. Brown, and N. Wood, 2004: A new parametrization of turbulent orographic form drag. *Quarterly Journal of the Royal Meteorological Society*, **130 (599)**, 1327–1347.

Bretherton, F. P., 1969: Momentum transport by gravity waves. *Quarterly Journal of the Royal Meteorological Society*, **95 (404)**, 213–243.

Broad, A., 2002: Momentum flux due to trapped lee waves forced by mountains. *Quarterly Journal of the Royal Meteorological Society: A journal of the atmospheric sciences, applied meteorology and physical oceanography*, **128 (584)**, 2167–2173.

Durran, D. R., 1995: Pseudomomentum diagnostics for two-dimensional stratified compressible flow. *Journal of the atmospheric sciences*, **52 (22)**, 3997–4009.

Eliassen, A., and E. Palm, 1961: On the transfer of energy in stationary mountain waves. *Geofys. Publ.*, **22**, 1–23.

Elvidge, A. D., and Coauthors, 2019: Uncertainty in the representation of orography in weather and climate models and implications for parameterized drag. *Journal of Advances in Modeling Earth Systems*, **11 (8)**, 2567–2585.

Georgelin, M., and F. Lott, 2001: On the transfer of momentum by trapped lee waves. case of the iop3 of pyrex. *J. Atmos. Sci.*, **58**, 3563–3580.

Héreil, P., and J. Stein, 1999: Momentum budgets over idealized orography with a non-hydrostatic anelastic model. i: Two-dimensional flows. *Quarterly Journal of the Royal Meteorological Society*, **125 (558)**, 2019–2051.

Howard, L. N., 1961: Note on a paper of john w miles. *J. Fluid Mech.*, **10**, 509–512.

Lott, F., 1998: Linear mountain drag and averaged pseudo-momentum flux profiles in the presence of trapped lee waves. *Tellus A: Dynamic Meteorology and Oceanography*, **50 (1)**, 12–25.

Lott, F., 2007: The reflection of a stationary gravity wave by a viscous boundary layer. *J. Atmos. Sci.*, **139**, 3363–3371, doi:http://dx.doi.org/10.1175/JAS4020.1.

Lott, F., 2016: A new theory for downslope windstorms and trapped lee waves. *J. Atmos. Sci.*, **73**, 3585–3597, doi:doi:10.1175/JAS-D-15-0342.1.

Lott, F., B. Deremble, and C. Soufflet, 2020a: Mountain waves produced by a stratified boundary layer flow. part i: Hydrostatic case. *Journal of the Atmospheric Sciences*, **77 (5)**, 1683–1697.

Lott, F., B. Deremble, and C. Soufflet, 2020b: Mountain waves produced by a stratified shear flow with a boundary layer. part ii: Form drag, wave drag, and transition from downstream sheltering to upstream blocking. *Journal of the Atmospheric Sciences*.

Lott, F., H. Kelder, and H. Teitelbaum, 1992: A transition from kelvin-helmholtz instabilities to propagating wave instabilities. *Physics of Fluids A*, **4**, 1990–1997, doi:http://dx.doi.org/10.1063/1.858368.

Lott, F., and M. Miller, 1997: A new subgrid scale orographic drag parameterization; its testing in the ecmwf model. *Quart. J. Roy. Meteor. Soc.*, **123**, 101–127.

Marshall, J., A. Adcroft, C. Hill, L. Perelman, and C. Heisey, 1997: A finite-volume, incompressible navier stokes model for studies of the ocean on parallel computers. *Journal of Geophysical Research: Oceans*, **102 (C3)**, 5753–5766.

Miles, J. W., 1961: On the stability of heterogeneous shear flow. *J. Fluid. Mech.*, **10**, 496–508.

Pithan, F., T. G. Shepherd, G. Zappa, and I. Sandu, 2016: Missing orographic drag leads to climate model biases in jet streams, blocking and storm tracks. *Geophysical Research Letters*, **43 (13)**, 7231–7240.

Ralph, F. M., P. J. Neiman, T. L. Keller, D. Levinson, and L. Fedor, 1997: Observations, simulations, and analysis of nonstationary trapped lee waves. *Journal of the atmospheric sciences*, **54 (10)**, 1308–1333.

Sandu, I., and Coauthors, 2019: Impacts of orography on large-scale atmospheric circulation. *npj Climate and Atmospheric Science*, **2 (1)**, 1–8.

Soufflet, C., F. Lott, and F. Damiens, 2019: Trapped mountain waves with a critical level just below the surface. *Quarterly Journal of the Royal Meteorological Society*, **145 (721)**, 1503–1514.

Steeneveld, G.-J., C. J. Nappo, and A. A. Holtslag, 2009: Estimation of orographically induced wave drag in the stable boundary layer during the cases-99 experimental campaign. *Acta Geophysica*, **57 (4)**, 857–881.

Teixeira, M. A., J. Argaín, and P. Miranda, 2013: Drag produced by trapped lee waves and propagating mountain waves in a two-layer atmosphere. *Quarterly Journal of the Royal Meteorological Society*, **139 (673)**, 964–981.

Tsiringakis, A., G.-J. Steeneveld, and A. Holtslag, 2017: Small-scale orographic gravity wave drag in stable boundary layers and its impact on synoptic systems and near-surface meteorology. *Quarterly Journal of the Royal Meteorological Society*, **143 (704)**, 1504–1516.